Advanced characterization of 2D materials using SEM image processing and machine learning

Mohamed Saib, Alain Moussa, Matteo Beggiato, Benjamin Groven,
Henry Medina Silva, Pierre Morin, Janusz Bogdanowicz, Gouri Sankar Kar,
and Anne-Laure Charley

imec, Celestijnenlaan 1, 3001 Leuven, Belgium

ABSTRACT

2D materials hold significant potential for enhancing semiconductor device performance. However, their integration necessitates the establishment of a robust metrology that is both accurate and fast, enabling a comprehensive understanding and precise control of their growth processes. Scanning electron microscopy (SEM) ticks all the boxes to be a promising technique for 2D materials characterization due to its sensitivity to monolayers (ML) and its high measurement throughput. Nevertheless, automating its measurement analysis is essential to avoid slow data processing and inaccuracies in results.

In this work, I propose a set of image-processing algorithms to extract various 2D material properties from SEM images and reveal hidden aspects of their growth processes. Firstly, I implemented and benchmarked two competing segmentation algorithms to process raw SEM images and localize surface regions corresponding to the substrate, 1ML, and 2ML. The first algorithm employs a statistical approach, named global thresholding, while the second is based on supervised machine Learning. These two algorithms were evaluated on a batch of wafers where tungsten disulfide (WS_2) material was grown, reaching a maximum of 2ML. The machine learning algorithm demonstrated exceptional performance, achieving segmentation success rates that surpassed 98%, outperforming the global thresholding technique, which has a success rate of 86.5%.

Subsequently, other algorithms were developed to extract quality indicators of 2D material layers from the segmented images, such as the coverage rate, and the count of basic crystals and islands. Reviewing all extracted properties enabled us to assess the process uniformity on wafers across different facets. On the other hand, the cross-analysis of these features unveiled some fundamental properties of the studied growth process. We determined the 1ML coverage at which crystals transition from a quasi-isolated growth to the coalescence phase, as well as when the formation of a uniform 1ML begins. Finally, we deduced the important relationship between the growth rates of 1ML and 2ML.

Keywords: 2D materials, Tungsten disulfide, SEM image segmentation, supervised machine learning, UNET

1. INTRODUCTION

Two-dimensional (2D) materials exhibit great potential for enhancing the performance of future semiconductor devices, spanning a variety of applications such as nano-electronics, nano-optoelectronics, and sensors [1,2,3,4,5,6,7]. This is achievable through the exceptional electronic, thermal, and optical properties of this new class of materials. For instance, the charge carrier mobility of 2D materials is several orders of magnitude higher compared to conventional bulk materials. Similarly, their optical properties can be precisely tailored to meet the specifications of the desired application. In bridging the transition from theoretical potential to practical implementation, the integration of 2D materials demands a meticulous adaptation process. Scientists face the challenge of aligning these materials with industry norms, particularly on 300 mm silicon wafers, all while ensuring the preservation of their impeccable characteristics.

To clarify the primary nature of 2D materials it is essential to provide a clear definition. Fundamentally, these materials refer to a class of materials characterized by an extremely thin morphology, typically consisting of one to a few layers thickness of atoms, confining their structure to a two-dimensional plane. The 2D confinement profoundly influences their crystalline lattice structure, thus dictating the arrangement of atoms and governing their electronic and structural attributes. The full potential of these materials is unlocked when are grown as a monocrystalline film. However, the transfer of growth techniques from R&D labs to 300mm wafers is not yet efficient as it results in numerous structural defects and poor thickness uniformity. In the fab environment, the growth of 2D materials remains complex and not well-controlled.

In recent years, researchers have concentrated their efforts on unraveling the growth mechanisms of ultra-thin layers to enhance their process control [8,9]. Generally speaking, the growth journey can be summarized with a few main steps (Figure 1). It starts with the nucleation phase where privileged locations emerge on the substrate surface. These locations can be either inherent to the substrate itself or introduced externally. Under normal conditions, the spatial distribution of nucleation sites is random and covers the entire wafer surface. The first atoms of the 2D materials come together at the nucleation sites to form stable nuclei. Subsequently, the growth phase initiates. This stage involves the in-plane expansion of nuclei by attaching new atoms to existing atomic structures, leading to the development of larger structures known as crystals. Considering various factors, 2D crystals can exhibit a diverse range of geometrical shapes, with triangular shapes being one of the most frequently observed. The orientation of crystals is an important feature in the interpretation of electrical behavior. At this stage, we can observe variations in crystal sizes across the wafer surface due to two main factors. Either nucleation occurs with some delay in certain locations, or the growth speed varies locally. It is worth noting that during this phase, individual crystals remain dispersed from one another.
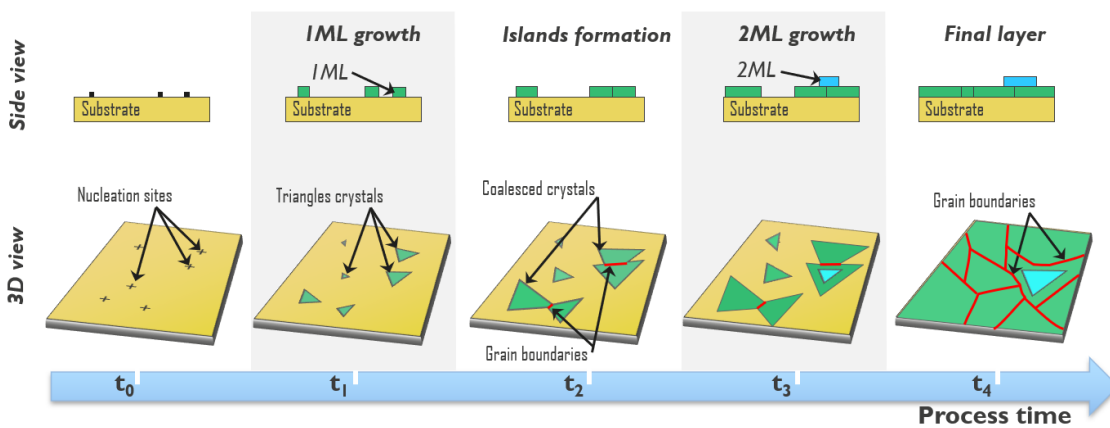

Figure 1: Schematic description of the growth process of 2D materials

The growth process continues in the 2D plan until the edges of adjacent crystals meet, resulting in the formation of continuous islands. This process is known as coalescence. When the orientation of the initial crystals is consistent, they

coalesce together, forming a monocrystal. Conversely, if the crystals have different orientations, the interface between them can generate defects known as grain boundaries. In this case, the formed island will take the shape of a mosaic of crystals. The resulting layer is then termed polycrystalline. Grain boundaries play a dominant role in degrading the electronic performance of the layer. As the first monolayer develops, certain process conditions may result in the inadvertent formation of nuclei and crystals beyond the intended 1ML. The growth and coalescence of these additional layers follow a similar mechanism as explained earlier and could lead to further degradation of mobility. On the other side, the expansion of the islands in the two-dimensional plane continues this process until a complete layer is formed. The optimization of the growth process relies on the iterative nature of trial-and-error-based experimental studies. In this context, metrology techniques play a pivotal role as they enable meticulous examination of samples, revealing all their crucial properties. Atomic Force Microscopy (AFM) has long been the cornerstone for studies on ultrathin layers due to its ability to offer a panoramic view into the nanoscale intricacies of materials. AFM is a high-resolution imaging technique that scans a sharp tip over a surface. The tip is affixed to a flexible cantilever, and as it traverses the surface, variations in forces between the tip and the sample are measured. These variations are then translated into a detailed, three-dimensional image with exceptional precision, providing comprehensive information about the topography and surface properties of the measured area. Nevertheless, this method faces challenges such as the slow measurement speed and the need for complex and expensive manual data processing. These factors give rise to multiple bottlenecks, compromising its scalability and confining it to qualitative studies.

In opposition to this, integration engineers consistently request more metrology data to enhance statistics, by expanding the inspected surfaces on one hand and measuring more wafers on the other. Given the current imperative of a shift towards quantitative measurements, alternative techniques have been tested, such as the Scanning Electron Microscope (SEM) [10]. SEM is extensively employed in the semiconductor domain and utilizes a focused electron beam to inspect the surface of a sample, generating signals such as Secondary Electrons (SE) and Back-Scattered Electrons (BSE). This metrology excels in delivering measurements with high lateral resolution (within the XY plane), typically 0.8nm; however, it is commonly recognized for its lower accuracy along the normal axis (Z-axis), particularly in determining thickness. Despite this apparent limitation, a recent study on 2D samples has revealed a direct correlation between the monolayers measured by AFM and the SEM gray levels (Figure 2) [11]. This discovery paves the way for the adoption of SEM as a viable alternative to AFM, promising a remarkable increase in measurement throughput, showcasing an impressive factor of 100 increase. However, it is crucial to emphasize that these benefits will only materialize after developing precise and rapid analysis tools for SEM measurements.
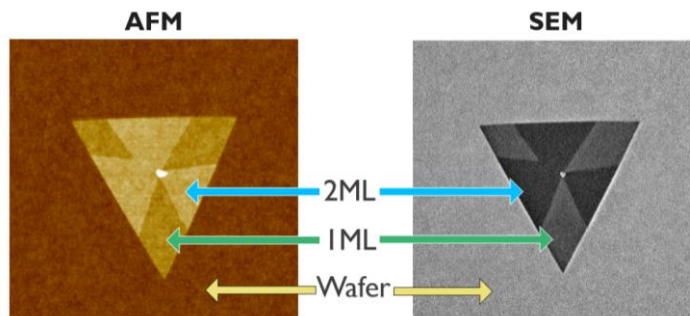

Figure 2: Images of an isolated WS_2 island taken with the metrology techniques AFM and SEM show a direct correlation between their measurements

This paper aims to introduce a suite of image-processing methods specifically designed for analyzing SEM measurements of 2D materials. These algorithms are meticulously crafted to extract as much meaningful information as possible about the studied samples and processes and within a reasonable time frame. Section 2 delves into the two image segmentation algorithms we developed during this project, employing statistical and machine-learning approaches. Subsequently, we conduct a rigorous benchmarking of these methods on a dedicated test dataset. In Section 3, we will show all the figures of merit of 2D materials that can be extracted from the processed images to obtain a comprehensive description of the samples. Following this, we delve into the analysis of the growth process based on the extracted data from SEM images. The conclusions will be drawn in Section 4.

2. SEM IMAGE SEGMENTATION

Image segmentation is an important step in measurement analysis, involving the partitioning of an image into uniform, non-overlapping, and homogeneous regions. Mathematically, this process includes the automatic classification of pixels from raw measurements into predefined categories before analysis. The outcome is the division of the image into multiple regions that represent various objects, simplifying the composition and facilitating an in-depth study of its components. Depending on the study's objectives, partitioning can be based on pixel intensity or surface texture. The literature offers a plethora of methods for this task, ranging from thresholding techniques to advanced approaches employing machine learning models. These diverse methodologies accommodate the multifaceted nature of application domains, enabling researchers to choose the most suitable approach based on their study's intricacies.

In this paper, the treated images are generated using the SEM technique. Despite its advantages, this metrology exhibits inherent limitations in its functioning, presenting challenges to image segmentation algorithms. The first limitation arises from the noise level, quantified by the signal-to-noise ratio (SNR) parameter. A low SNR of an image indicates a high noise level, complicating the discrimination of pixels among different segmentation classes. To enhance the SNR, we applied systematic Gaussian filtering to the images, carefully choosing the kernel width to minimize noise without compromising the crystal structures' contrast. The second limitation is associated with non-uniform image backgrounds. Segmentation algorithms are highly sensitive to pixel intensities, making them susceptible to misclassification in the presence of small distortions in the background. To address this issue, we decided to calculate the average of all normalized SEM images and then invert it to obtain the distortion correction coefficient. This coefficient is subsequently applied to images one by one before their segmentation operation.

In this study, we developed two competitive segmentation algorithms to process SEM images. The first one relies on a global thresholding method, while the second employs a supervised machine learning algorithm.

2.1 Segmentation based on global thresholding:

The segmentation using the global thresholding approach stands out as one of the most widely employed techniques, owing to its compromise between implementation simplicity, robustness, and efficient computation [12,13]. This method capitalizes on the statistical properties of an image, where distinct regions exhibit different pixel intensities. In the fundamental scenario of bimodal segmentation, often termed binarization, the optimal threshold value is set at the midpoint between the intensities of the two distinct regions constituting the image. This is typically determined by analyzing the envelope of the intensity histogram, with each specific region represented by a peak. It is generally assumed that these peaks follow a Gaussian distribution shape. To address the weighting of regions represented with small peaks, we opted to analyze the histogram envelope at the logarithmic scale. When the histogram encompasses multiple peaks, multiple thresholds are calculated in a process known as image segmentation. The Otsu method is one of the most famous techniques for threshold determination, however, it is computationally expensive, particularly when the number of segments exceeds 2 [14]. Otsu's method proves impractical for threshold selection in the multimodal case due to its slow computation time.

Figure 3(a) presents the envelopes of six histogram examples of SEM images selected in pairs from three test wafers. We can distinguish three separated ranges of grayscale values corresponding to regions: the substrate surface, 1ML, and 2ML of the 2D material (Figure 3(b)). The six envelope shapes exhibit considerable variation based on growth conditions, posing a challenge for threshold determination. In certain configurations, the substrate and 2ML appear as peaks, while in other cases, they manifest as simple shoulders. These shoulders arise in two scenarios: firstly, when objects are rare in the SEM image, and secondly, when the typical grayscales of two different objects in the images are very close compared to the width of their distribution. Threshold determination is also impacted by intensity fluctuations between two SEM images, potentially caused by the autofocus step performed by the SEM tool before image acquisition. The combination of these factors expands the ranges where thresholds must be positioned to 15% and 29% of the total intensity for thresholds 1 and 2, respectively. In summary, the dynamic determination of thresholds must be robust to variations in histogram shapes and intensity shifts.

To address these challenges, we have implemented adaptive automatic threshold calculation. The process begins with the acquisition of the image histogram. Following this, the envelope curve is extracted and smoothed to eliminate minor local

fluctuations. Subsequently, the envelope content is determined by fitting a multimodal function, specifically, a sum of three Gaussian probability density functions representing the substrate, 1ML, and 2ML. Finally, thresholds are determined at the intersections between the fitted distributions. This approach is both fast and scalable, leveraging the server's computing capabilities.
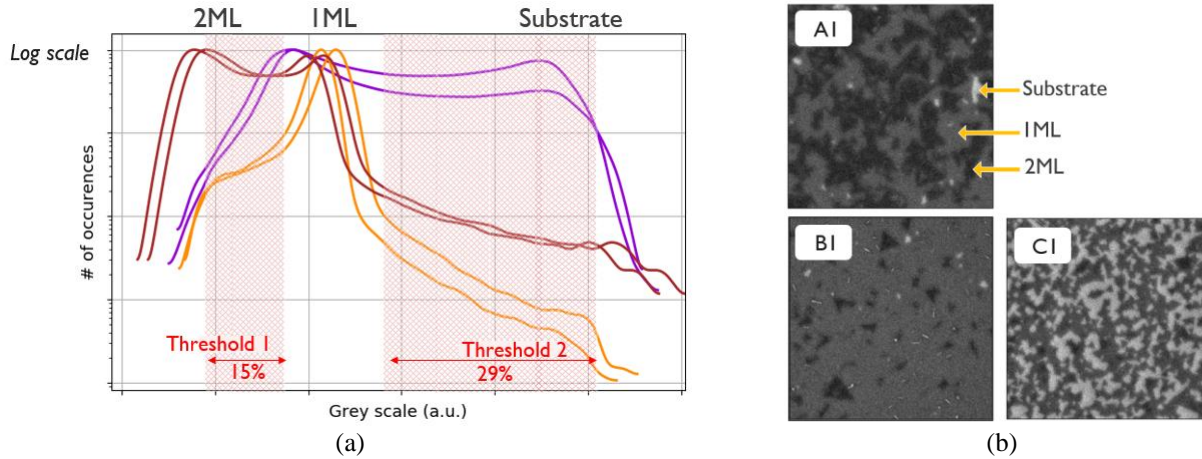

Figure 3: (a) Histograms of a collection of six SEM images, representing by pair three distinct process conditions. (b) Example of SEM images taken from 3 process conditions A, B and C

2.2 U-NET-Based Image Segmentation:

The second approach implemented in this study employs a supervised machine learning method known as U-Net. In contrast to the global thresholding method, U-Net is designed to learn image segmentation without predefining threshold values. This model is popular because it exhibits a high ability to accurately segment objects, even when they are small, have irregular shapes or the training dataset is small [15,16]. The architecture of U-NET is composed of two main blocks: an encoder and a decoder (Figure 4). The encoder aims to capture hierarchical features from the input image, while the decoder is responsible for the restoration of spatial information. The basic concept behind the encoder is to use a series of convolutional layers that progressively down-sample the input image having the size 256 x 256 pixels^2. Each layer encompasses multiple 3×3 convolutional kernels followed by the Sigmoid activation function and a 2×2 max pooling operation with the stride of 2. At each down-sampling step, the number of convolutional kernels is doubled. The encoder decreases the spatial resolution of the image until it reaches the model bottleneck, generating the compressed representation of the input. The decoder block takes these compact data and applies a series of up-convolutional layers to gradually regenerate the desired segmented maps. To facilitate image reconstruction with all small details, a series of skipped connections are used to transfer low-level image properties from the encoder layers to their reciprocal decoder layers. This allows the decoder to recover the spatial resolution of the image while maintaining the extracted features. The output image is the same size as the input and contains 3 discrete levels, 0 for the substrate surface, 1 for the 1ML, and 2 for the 2ML.

Practically, the U-Net model requires cutting input SEM images of 1024x1024 pixels^2 into smaller pieces, 256 pixels^2 to serve a few limitations. Firstly, reducing the substantial memory requirements associated with the model training. This division allows for more efficient training and inference on hardware with limited memory. Additionally, breaking down large images into smaller patches helps mitigate computational load. Training on smaller patches facilitates parallel processing, leading to faster training times and making it easier to distribute the workload across multiple GPUs or processors. During the inference process, it is crucial to emphasize that the small simulated patches are assembled to reconstruct the segmented image, maintaining an identical field of view as the SEM. This processing strategy proves practical for effectively handling large-scale image data in segmentation tasks. As with all supervised machine learning models, the UNET is trained on a subset of the SEM data and then tested on a different portion. During training, the algorithm learns patterns from a specific dataset, and testing assesses its ability to generalize those patterns to new, never

seen data. This separation helps in fine-tuning the model structure and its hyperparameters, helping to avoid overfitting and gauging its effectiveness in real-world scenarios.

Traditionally, the proportion of training and test datasets is 80% and 20%, but in this work, we dedicated half of the data to the training and the second half to the validation. The hyperparameters we used for our model are, the Adam optimizer with a learning rate of 1e-2, a batch size of 12 images, and Mean Squared Error (MSE) as a loss function. Initiating the training of a new model involves the use of randomly selected initial weights, which can prolong the model's convergence to its optimal configuration. To accelerate the training, we employed a three-phase strategy. Firstly, we shuffled the training dataset and started the model training on only 20% of the data. Upon achieving a satisfactory configuration, we increased the data portion to 50%, broadening the range of cases considered. This intermediate configuration was further refined by training on the entire training dataset. This staged approach facilitated the model calibration and reduced its training time.
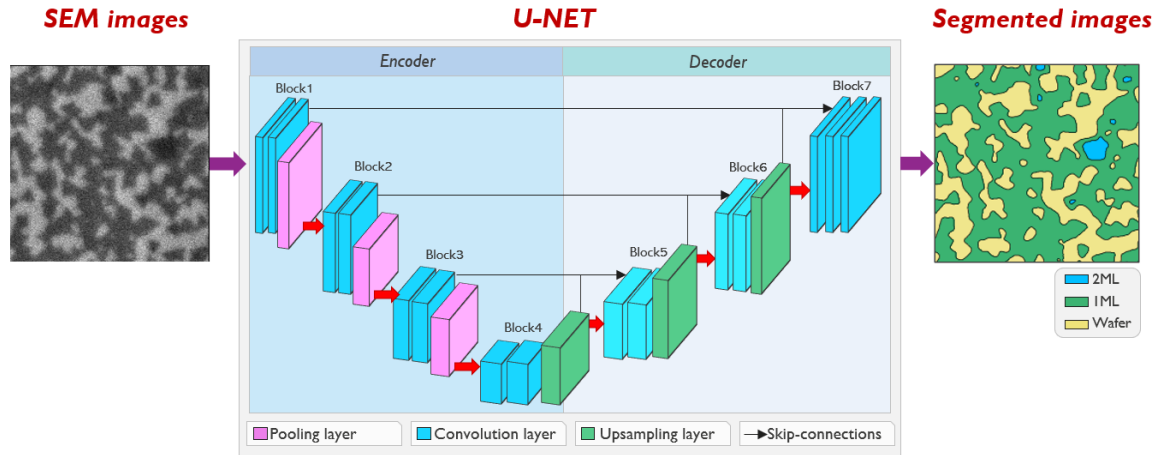

Figure 4: Schematic of the U-NET model
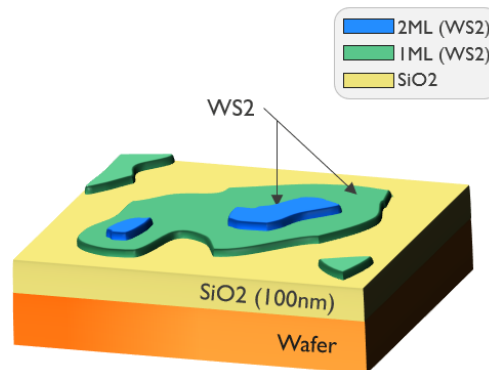
2.3 Segmentation performance:

Figure 5: Stack description of the 2D materials samples

The experimental validation of the segmentation algorithms has been conducted on tungsten disulfide (WS_2) 2D materials, having a maximum of 2 ML grown of 100nm SiO2 layer (Figure 5). The experimental setup employed a comprehensive Design of Experiments (DOE), encompassing a total of 6 wafers processed in pairs and subjected to three distinct growth conditions denoted as A, B, and C (Table 1). These varying growth conditions resulted in the creation of WS_2 layers with different geometric configurations and number of MLs. Each wafer in the dataset has been measured with the SEM tool, capturing a total of 89 locations for analysis. The acquired images have a nominal size of 1024x1024 pixels². The cutting of raw SEM images into pieces sized 256x256 pixels, compatible with the U-Net model, has resulted in a total dataset of

8544 images. Given this high number of images, we did not resort to data augmentation. As previously mentioned, half of this data was allocated to the training set, while the second half was assigned to the validation set. The full dataset not only offers a diverse range of WS_2 layer configurations but also ensures a robust evaluation across multiple growth conditions, providing a rich and comprehensive basis for the thorough examination and validation of the two employed segmentation methodologies.

Wafer	Target layer	Process
A1	1ML	Setup 1
A2	1ML	Setup 1
B1	1ML	Setup 2
B2	1ML	Setup 2
C1	2ML	Setup 3
C2	2ML	Setup 3

Table 1: Design of Experiment for the image segmentation study

To evaluate the segmentation performance of the two algorithms, all input SEM images were initially manually segmented. This process entailed a person visually identifying thresholds and labeling different features within the images. We chose manual processing for the generation of ground truth data to guarantee the precision and accuracy of the reference dataset. The segmentation quality of the algorithms was assessed on the entire dataset by calculating the ratio of the number of pixels assigned to the correct category over the total number of pixels. The closer this score is to 100%, the better the performance of the algorithms.

Figure 6 presents three SEM images randomly selected from wafers A2, B2, and C2, along with their segmented images using two techniques: global thresholding and the U-NET model. The results obtained through the global thresholding approach effectively capture prominent structures, representing the 1ML. However, there is a noticeable dilatation of the 1ML or 2ML areas, depending on the specific cases. This is indicative of a slightly imprecise threshold adjustment. Additionally, the method reveals multiple small structures that are not clearly visible in the raw measurements, possibly induced by the noise in the SEM images. The conjunction of three factors, low signal-to-noise ratio (SNR) in SEM images, a small difference in gray levels between 1ML and 2ML, and objects appearing in the histograms as shoulders create some ambiguous boundaries between regions, degrades a bit the segmentation performance. The accuracy of this technique compared to the reference varies in the range of 79.5% to 92.9% across the 6 studied wafers (Figure 7).

The U-NET model has undergone training for segmentation, with meticulous attention paid to the quality of both the training and validation datasets. Recognizing that the model's efficacy hinges on the chosen split strategy, we have deliberately employed a methodology where one wafer per condition (wafers A1, B1, and C1) is utilized for training, while the second set of wafers (A2, B2, and C2) is reserved for the evaluation of the unbiased performance. This approach is aimed at ensuring a robust and representative training regimen to enhance the model's overall performance. The segmented images by the U-NET model exhibit a very good quality where results in all cases are very close to the ground truth. According to Figure 7, the segmentation performance of this supervised model reached on the training data set a score of 99.6%. This high score could mean that the model is overfitting. This occurs when a model performs well on the training data but fails on data not seen before. In the case of this study, the U-NET model shows an accuracy score of 98% on the validation images, indicating that overfitting is not occurring. Our investigations revealed that 2% of errors are happening exclusively at the contour level where only a few pixels are assigned to the wrong category compared to the reference. It is crucial to note that no region, no matter how minuscule the region, has been misclassified. Considering the outstanding performance of the U-Net model, all segmented images presented in the remainder of this paper will be exclusively generated by it.
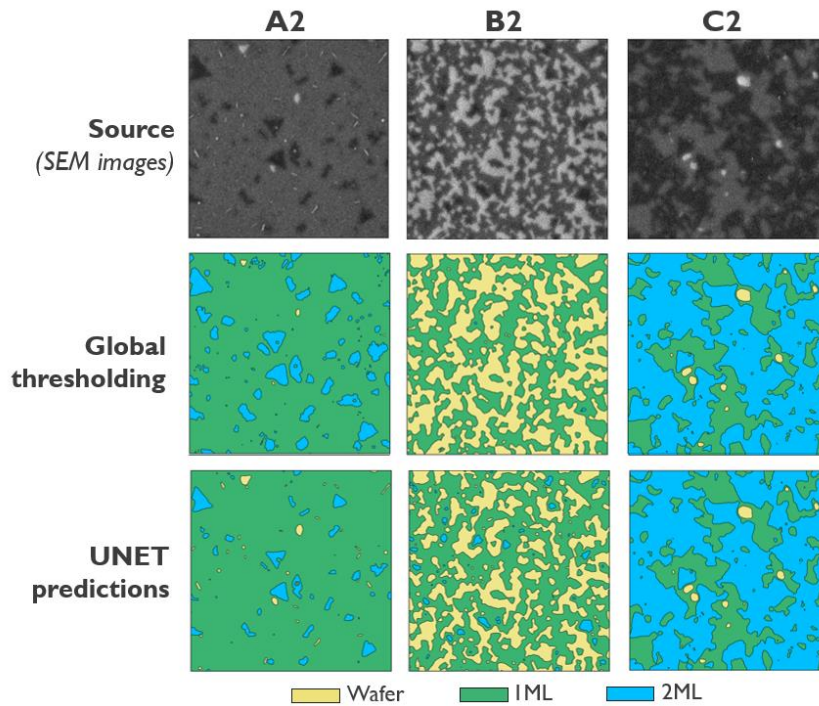
Figure 6: Example of raw SEM images taken from samples A2, B2, and C2 as well as their respective segmentation with the global thresholding and UNET approaches
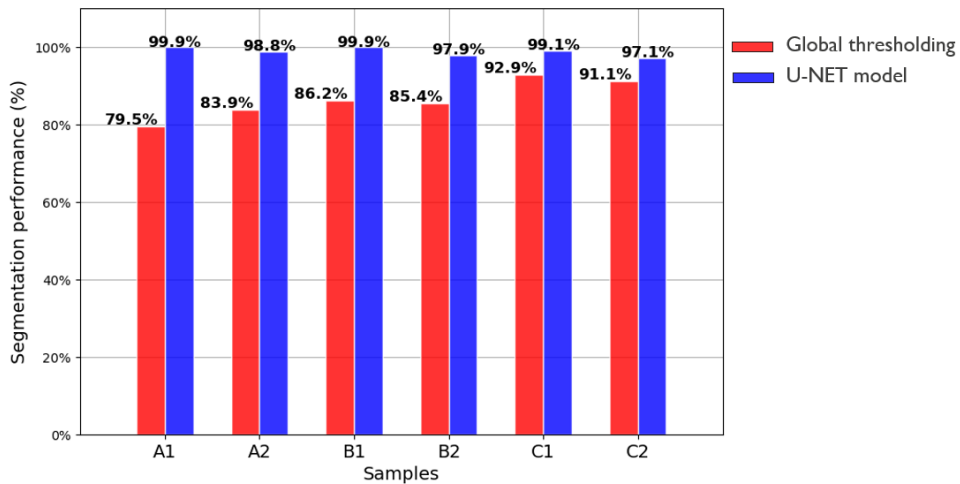

Figure 7: Bar graph representing the performance of image segmentation of Global thresholding and U-NET approaches calculated by comparison with reference data generated manually

3. Study of 2D material growth process:

3.1 Images postprocessing:

Postprocessing of segmented images is of utmost importance as it enables us to determine the figure of merit for the studied samples. In this section, our primary objective is to facilitate the quantitative characterization of 2D materials by generating numerical metrics that accurately describe various aspects of their local properties. For the first characteristic, we measured the coverage rate of grown 1ML and 2ML from the segmented images. The coverage parameter reflects the degree to which the thin film has developed on the substrate. The coverages of 1ML and 2ML are relevant for directing the optimization of the growth process of 2D materials. The coverage is reported as the percentage of the monolayer area over the total surface of the SEM image. Ideally, the coverage of 2D materials is 100% for 1ML and 0% for 2ML. Additionally, we quantified the properties of the 2D material islands by determining their count, orientation, and area (Figure 8). We also computed the variability of both orientation and surface over the field of view (FOV) because they offer crucial insights into local process variability. To explore further facets of the growth process, we implemented an algorithm that allows us to identify elementary crystals even within islands, i.e., coalesced regions. This algorithm reduces iteratively the size of islands through numerical erosion until individual crystals that compose them are separated, enabling us to count them. This approach provides an estimation of the number of crystals when the processed layer has openings between islands. Consequently, we can compute the coalescence rate of crystals as the ratio of the count of islands over the count of crystals. This parameter indicates, on average, how many crystals merged to form islands in the processed SEM image.
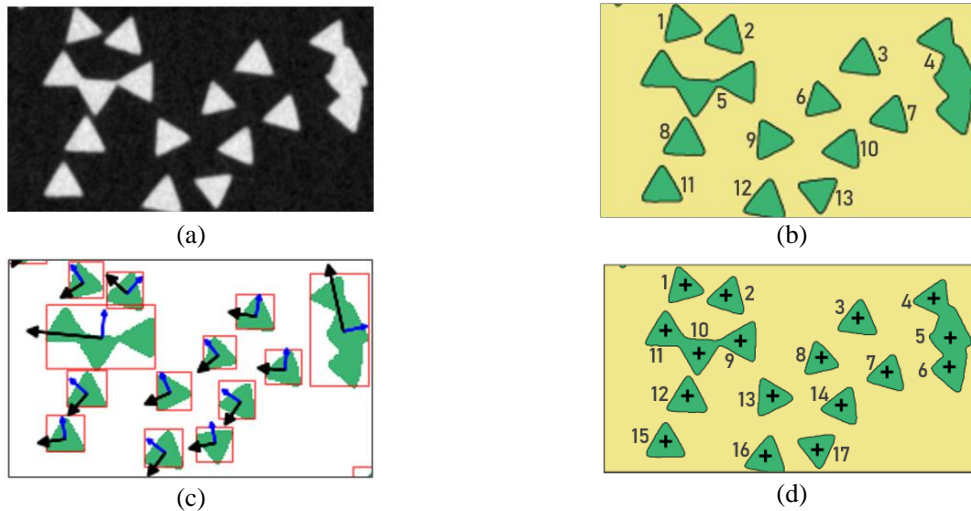

Figure 8: (a) Segment of an SEM image depicting a cluster of 2D material crystals with triangular shapes. (b) Enumeration of islands. (c) Orientation analysis of islands. (d) Tally of individual crystals identified through erosion calculations.

3.2 Design of Experiment:

The objective of this section is twofold. Firstly, to evaluate the uniformity of the process across the surfaces of the wafers, and secondly, to ascertain key properties of different phases in the growth process of 2D materials, ranging from the critical nucleation step to the growth of 2 ML. This exploration is conducted through the implementation of a second Design of Experiment (DOE), utilizing a new set of wafers labeled D01 to D04, spanning four growth durations of the WS2 layer. D1 corresponds to the shortest growth time, while D04 to the longest (Figure 9). The growth time for D02 and D03 is in between the 2 extreme configurations. The modulation in growth time results in a significant variation in the grown layers of 2D materials. All wafers have been examined by SEM across 89 measurement sites, covering their entire surface.

Similarly, to the first DOE, the SEM images have a field of view (FOV) of 1024x1024 pixels². All SEM images are first segmented and later preprocessed to generate all their local properties.
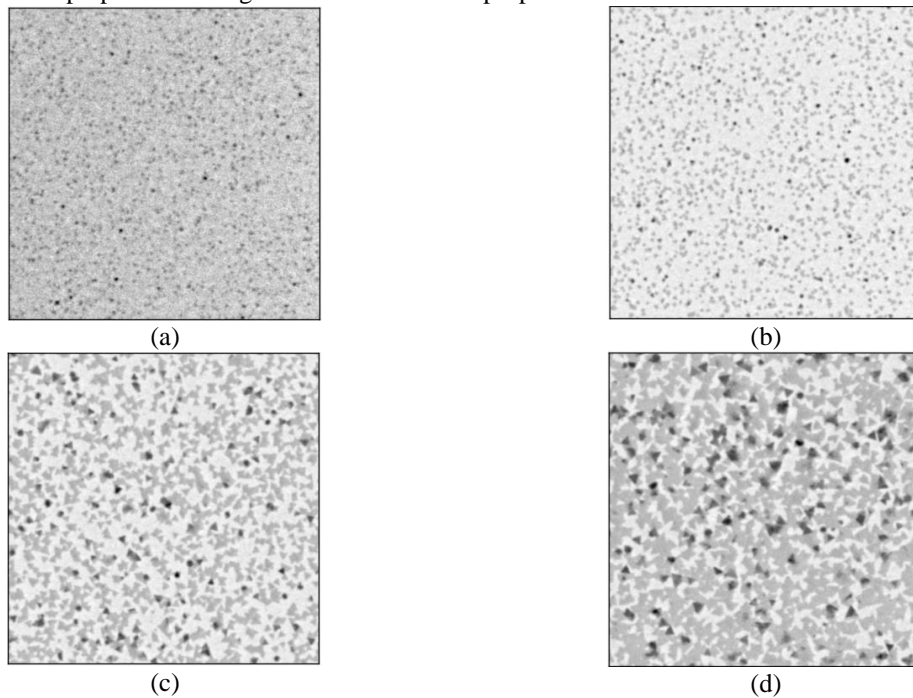

Figure 9: SEM images depict WS_2 thin films grown on the wafers D01 to D04 where the growth time varies from the shortest (a) t1, through (b) t2, (c) t3, to the longest (d) t4.

3.3 Results and discussion:

All raw SEM images from wafers D01 to D04 have been systematically segmented and post-processed using a standard laptop. Despite this, the data processing duration has remained reasonable, averaging around 10 seconds per image. Consequently, the total processing time per wafer is approximately 16 minutes. It is worth mentioning that the scalability of our analysis scripts presents a substantial opportunity for a significant reduction in processing time (by an x-factor) when executed on a High-Powered Computing (HPC) server.
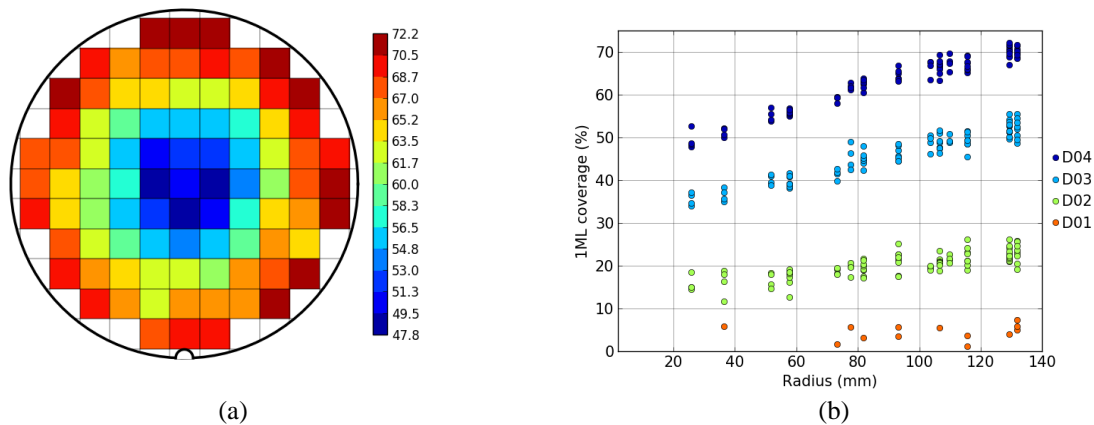

Figure 10: (a) Wafer map showing the 1ML coverage for the wafer D04, (b) Scatterplot of 1ML coverage plotted as function of the radius for wafers D01, D02, D03, and D04

The results of the data analysis enable us to comprehensively evaluate the quality of the 2D material-grown layers of WS$_2$, utilizing various extracted metrics. First, in Figure 10 (a), we present the wafer map illustrating the 1ML coverage of WS$_2$ for wafer D04. A radial fingerprint is observed in this representation, where the coverage is low at the wafer center (47.8%) and sharply increases at the wafer edge, reaching 72.2%. This indicates that the uniformity (3σ) of 1ML coverage is relatively weak, corresponding to 19.5%. Figure 10 (b) depicts the 1ML coverage plotted as a function of the radius for the 4 DOE wafers. It is evident that the uniformity from center to edge is optimal for wafer D01 and gradually degrades with increasing growth time until reaching the worst case for wafer D04. This suggests that the primary cause of the low coverage uniformity is the growth process itself, rather than nucleation, as longer growth times lead to poorer coverage uniformity.

We are showing in Figure 11, 3 additional characteristics extracted for the wafer D04. Figure 11 (a) depicts the wafer map displaying the count of 1ML islands. We observe a radial fingerprint of the islands' count but with an inverted amplitude in comparison with the 1ML coverage. The maximum number of islands is 175, and available at the center of the wafer. This island's count gradually decreases when we move towards the wafer edge, reaching a minimum of only 9 islands. Figure 11 (b) shows the wafer map of the count of individual crystals pinpointed by image erosion of 1ML islands. The crystals count also has a radial fingerprint with a maximum number at the wafer center with 691 crystals and it decreases gradually to reach a minimum of 523 crystals at the wafer edge. This map indicates that the 1ML crystal formation is 32% more efficient at the center of the wafer than its edge. The characterization of this property is of great interest since it allows the assessment of the process control of crystal distribution over the wafer surface. Figure 11 (c) represents the coalescence rate of the 1ML. This parameter is calculated as the ratio between the number of islands over the number of crystals. The wafer map also shows for this property a radial fingerprint where the crystal coalescence rate is on average 3.8 at the wafer center and it increases above 40 at the wafer edge. When we cross the coalescence rate with the 1ML coverage, we deduce the coalescence rate increases when the coverage increases and vice versa. This suggests the crystal's growth process is one of the main contributors to the coalescence rate in the studied samples.
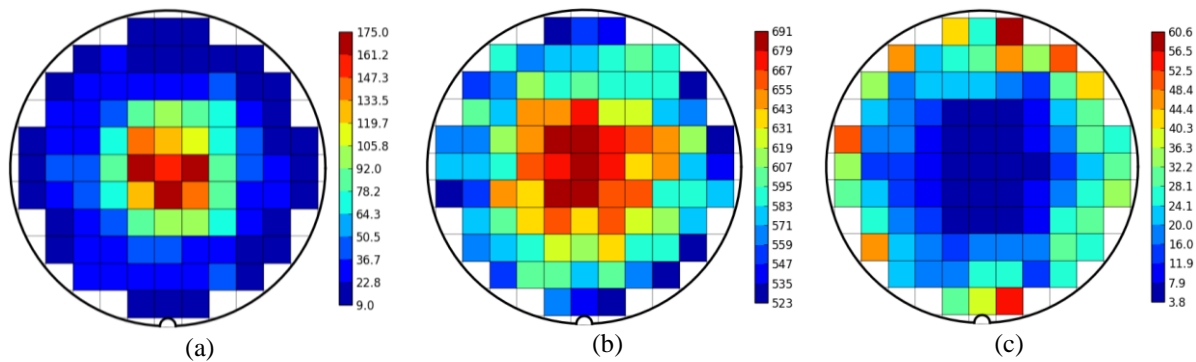

Figure 11: Wafer maps showing for the wafer D04, (a) Count of the 1ML islands, (b) Count of the 1ML crystals, (c) coalescence rate of 1ML crystals

Before we continue the properties analysis of the 2D materials samples, let's delve into some theoretical concepts. The nucleation and growth of 2D materials remains not sufficiently understood as we hope. Nevertheless, it exists in the literature various theoretical models that attempt to explain it, such as Volmer-Weber [17], Stranski-Krastanov [18], and LaMer-Dinegar [19]. The LaMer-Dinegar model offers a simple yet insightful framework for describing the fundamental principles of nucleation and growth in materials (Figure 12). This theoretical approach posits that the growth of crystals unfolds in three separate stages: atom formation, nucleation, and crystal growth. This process is described with the green curve. In the first phase, the growth chamber is intentionally prepared to be supersaturated with material that will form the nanoparticles. Above a certain concentration of atoms, the second phase starts. Nucleation then occurs as small clusters aggregate to form stable nuclei. These nuclei will be attached to the substrate surface, preferentially at the defects, or nanoparticles. The growth of these nuclei continues until getting the first crystals which marks the start of the third and last phase, the growth. The LaMer-Dinegar model suggests that the nucleation process completely stops to allow the growth process. This means that the count of nuclei will not increase anymore on the substrate surface. The crystals' growth is

facilitated by the addition of atoms at their edges, achieved through processes like diffusion and cluster coalescence. To connect the LaMer-Dinegar model to our study, we incorporated the blue curve into Figure 12, representing an illustration of the count of 2D material islands on the substrate surface. The count of crystals starts at 0 during the atom generation phase, as they are not yet adhered to the wafer surface. The number of nuclei sharply rises during the nucleation phase as clusters form separated regions. By the end of this nucleation phase, the count of nuclei reaches its maximum. This number remains constant at the beginning of the growth regime until the first coalescences occur, leading to the formation of islands. The width of the plateau corresponding to this phase could be more or less wide. A wide plateau indicates that nuclei are spatially very far from each other, requiring a long growth time for coalescence. In contrast, a narrow plateau occurs when the density of nucleation is high, meaning the distance between nuclei is small. Finally, when the crystals' coalescence starts, the number of islands gradually decreases because multiple crystals will shape a single island. This process continues until forming a single large island or a complete layer.
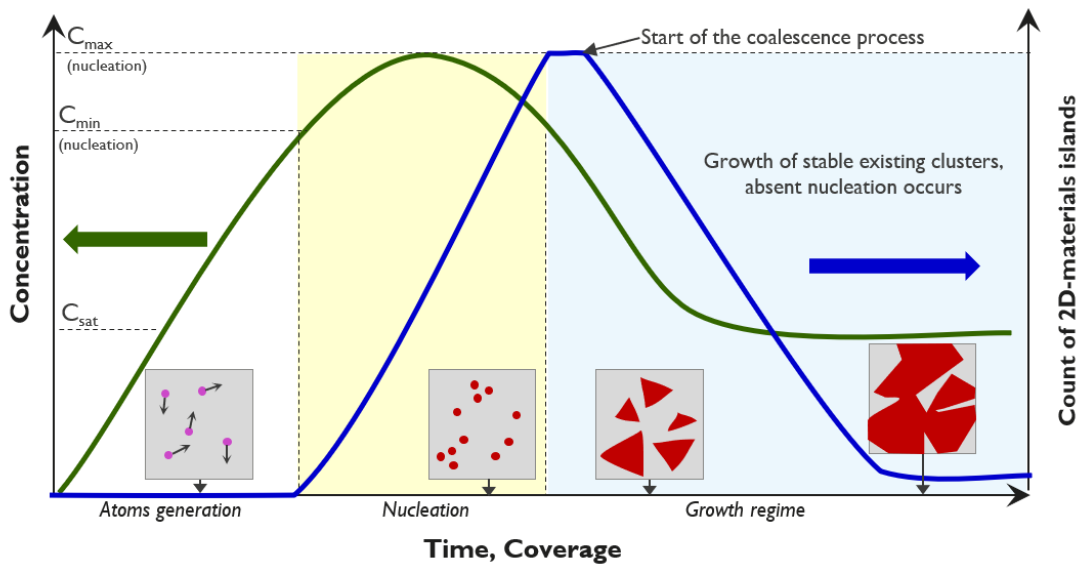

Figure 12: The LaMer-Dinegar model describes, with the green curve, the growth process of layers through three stages: atom formation, nucleation, and crystal growth. The blue curve illustrates the count of 2D materials islands throughout the process stages

Figure 13 illustrates the count of 2D material islands as a function of 1ML coverage, computed on the DOE wafers. Within this intricate dataset, two distinct and noteworthy trends emerge. Below the 8% coverage threshold, the incremental increase in coverage, even if marginal, correlates with a significant rise in the number of nuclei. This empirical observation strongly suggests that we are in the nucleation process phase. This is why it contribution to the coverage is high. This gives echo the nucleation phase outcomes predicted by the LaMer-Dinegar model. Further corroboration of these findings comes from the examination of a segmented SEM image of wafer D01. The visual analysis confirms that nucleation sites are numerous and spatially separated, providing a concrete explanation for the observed high count of islands during this phase. Above the 8% coverage, the count of islands exhibits an opposing trend to before. Delving into the dataset from wafers D02, D03, and D04, we discern that each contributes unique insights representing a subset of the overarching diminishing trend. The count of islands undergoes a gradual, monotonic decrease, resulting from the progressive formation of a single large island or layer. This phase is characterized by the coalescence process of islands, leading to a reduction in their overall count. It is noteworthy that no change in the slope is detected above 8% coverage, confirming that the nucleation process is not taking place. We note also that no plateau exists in the curve of count of islands between the nucleation and coalescence phases, meaning the crystals merging starts immediately with the growth of crystals. These results align with the predictions derived from the LaMer-Dinegar model.
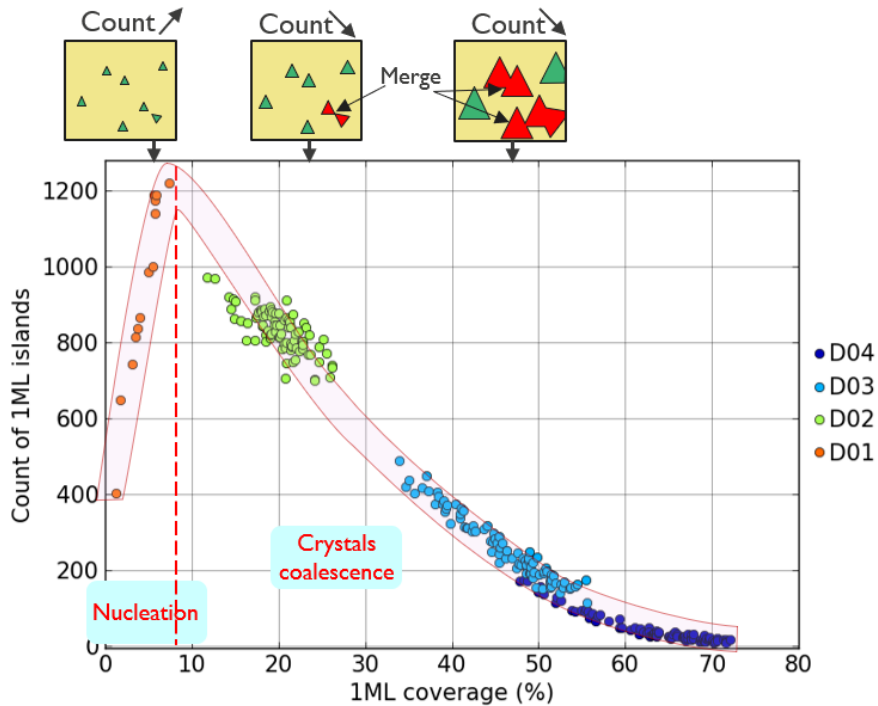
Figure 13: Scatterplot showing the count of the 1ML crystals as a function of 1ML coverage for wafers D01 to D04
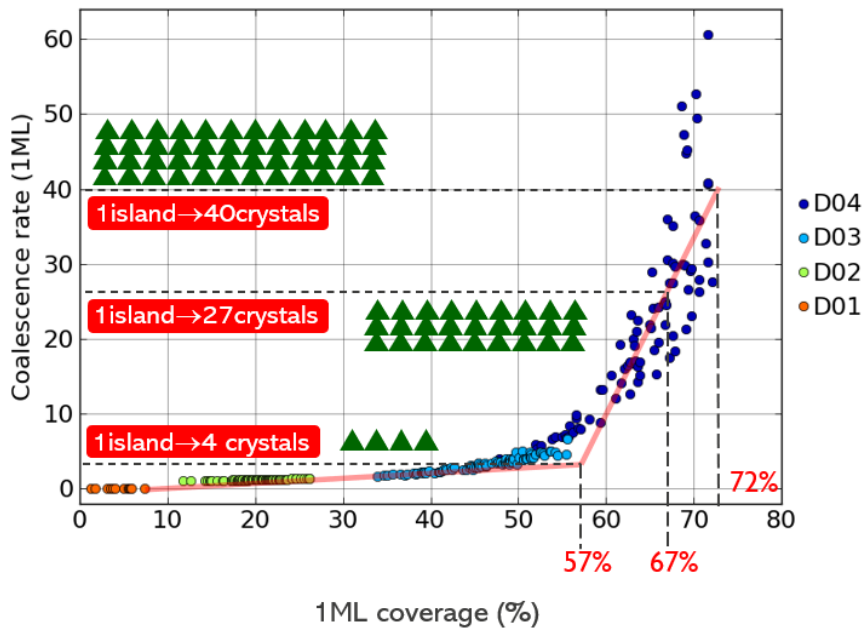

Figure 14: Scatterplot showing the coalescence rate of the 1ML crystals as a function of 1ML coverage for wafers D01 to D04

Figure 14 illustrates the coalescence rate of crystals as a function of the 1ML coverage for wafers D01 to D04. Two distinct phases are discernible in this curve. Within the coverage range of [1%, 57%], the coalescence rate exhibits a linear increase, characterized by a modest slope of 7%. This small rate is attributed to the substantial spacing between the 1ML islands, resulting in a low coalescence probability. As an illustration, islands are composed of only 4 neighbor crystals when the 1ML coverage is 56%. However, beyond the 57% coverage threshold, the diminishing space between islands becomes conducive to more coalescences. The coalescence rate experiences a significant acceleration marked by a steep slope of

29%. This abrupt change in slope underscores a notable transition in the growth dynamics. The beginning of the second phase marks the time when the 1ML starts to be shaped. It is noteworthy that alternative configurations of the growth process might yield different threshold values compared to those observed here. The presence of only two regimes in the coalescence rate curve suggests a quasi-uniform distribution of nuclei across the substrate. To explore hypothetical scenarios, let's consider an ideal uniform distribution of nuclei with consistent crystal growth, which would shift the threshold between the two regimes to a higher coverage, possibly close to 99%. Conversely, a non-uniform distribution of nuclei, such as dense clusters separated by large spaces, would result in a different shape for the coalescence rate curve. The absence of a third regime reinforces the conclusion that nuclei are spatially quasi-uniformly dispersed, contributing to the stability and predictability of the observed coalescence rate. This insight deepens our understanding of the intricate interplay between 1ML coverage and coalescence dynamics in the growth process of 2D material islands on the substrate. Controlling the growth of 2D materials at the monolayer level is essential for achieving high-quality devices. This involves ensuring a meticulous sequencing of growth, where the initiation of a new 2D material monolayer occurs only after the completion of the previous one. To evaluate the monolayer control for the studied process, we are showing in Figure 15, the coverage of the 2ML evolution as a function of the 1ML. We observe on average, for a 1ML coverage lower than 12%, there is no growth of the 2ML. Above this limit, the 2ML begins its growth. The 2ML coverage increase is proportional to the increase of 1ML coverage. The 2ML generation is 22% compared to 1ML. This indicates the control of the process growth on the DOE wafers is bad since the 2ML starts growing at an early stage of the 1ML growth. In addition to that, the 2ML generation rate of 22% is high because each 10% increase in the 1ML coverage, will induce a 2.2% increase in the 2ML coverage.
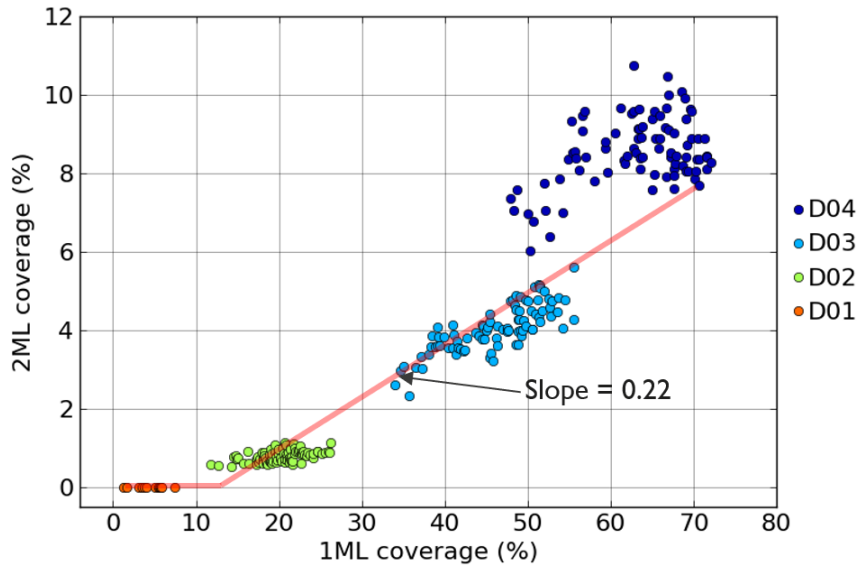

Figure 15: Scatterplot showing the 2ML coverage as a function of 1ML coverage for wafers D01 to D04

4. SUMMARY AND CONCLUSIONS

In this paper, we proposed a set of algorithms allowing processing the of SEM images and extracting important 2D materials properties. We first implemented and compared two image segmentation algorithms for the analysis of SEM measurements. The two techniques employed are a global thresholding approach and a U-NET model. The analysis of experimental results revealed that the U-NET model is significantly more efficient, with a segmentation success rate exceeding 98% on both the training and validation datasets compared to an average of 86.5% for the global thresholding approach. Subsequently, we conducted post-processing on the segmented images and quantified various properties of the WS2-grown crystals and islands. These data allowed us to assess the process uniformity of multiple properties across the wafer surface. The cross-analysis of these sample features enabled us to identify some hidden growth process signatures, such as nucleation, growth, and coalescence phases.

REFERENCES

[1]: B. Liu, Y. Chen, C. You, Y. Liu, X. Kong, J. Li, S. Li, W. Deng, Y. Li, H. Yan, and Y. Zhang, High performance photodetector based on graphene/MoS2/graphene lateral heterostrurcture with Schottky junctions, Journal of Alloys and Compounds, Volume 779, 30 March 2019, Pages 140-146

[2]: R. K. Prasad, K. Ghosh, P. K. Giri, D.-S. Kim, D. K. Singh, High-Efficiency Photodetector Based On CVD-Grown WS2 Monolayer, CS Appl. Electron. Mater. 2023, 5, 7, 3634–3640

[3]: M.F. Craciun, S. Russo, M. Yamamoto, S. Tarucha, Nano Today, (2011), Volume 6, Issue 1, Pages 42-60

[4]: J. Z. Hassan, A. Raza, Z. U. D. Babar, U. Qumar, N. T. Kaner and A Cassinese, 2D material-based sensing devices: an update, J. Mater. Chem. A, 2023, 11, 6016-6063

[6]: H. Ying, X. Li, H. Wang, Y. Wang, X. Hu, J. Zhang, X. Zhang, Y. Shi, M. Xu, Q. Zhang, Band Structure Engineering in MoS2 Based Heterostructures toward High-Performance Phototransistors, Advanced optical materials, Volume8, Issue13, July 6, 2020, 2000430

[7]: V. Faramarzi, V. Ahmadi, M. T Hwang, P. Snapp, Highly sensitive crumpled 2D material-based plasmonic biosensors, Biomed Opt Express, 2021 Jun 29;12(7):4544-4559

[8]: X. Tong, K. Liu, M. Zeng, L. Fu, Vapor-phase growth of high-quality wafer-scale two-dimensional Materials, 2019, InfoMat. 2019;1:460–478

[9]: X. Xu, K. Liu, Progress and perspective on the growth of two-dimensional single crystals Science Bulletin 67 (2022) 1410–1412

[10]: H. Hiura, H. Miyazaki, K. Tsukagoshi, Determination of the number of graphene layers: discrete distribution of the secondary electron intensity stemming from individual graphene layers, Appl. Phys. Express, 3 (2010), Article 095101, 10.1143

[11]: A. Moussa, J. Bogdanowicz, B. Groven, P. Morin, M. Beggiato, M. Saib, G. Santoro, Y. Abramovitz, K. Houtchens, S. Ben Nissim, N. Meir, J. Hung, A. Urbanowicz, R. Koret, I. Turovets, G. F. Lorusso, A.-L. Charley, "300mm in-line metrologies for the characterization of ultra-thin layer of 2D materials," Proc. SPIE 12496, Metrology, Inspection, and Process Control XXXVII, 124961X (27 April 2023);

[12]: F. Yan, H. Zhang, C.R. Kube, A multistage adaptive thresholding method, Pattern Recognit. Lett., 26 (2005), pp. 1183-1191

[13]: D.-M. Tsai, A fast thresholding selection procedure for multimodal and unimodal histograms, Pattern Recognit. Lett., 16 (1995), pp. 653-666

[14]: N. Otsu, A Threshold Selection Method from Gray-Level Histograms, EEE TRANSACTIONS ON SYSTREMS, MAN, AND CYBERNETICS, VOL. SMC-9, NO. 1, JANUARY 1979

[15]: O. Ronneberger, P. Fischer, T. Brox, U-net: Convolutional networks for biomedical image segmentation, International Conference on Medical Image Computing and Computer-Assisted Intervention, Springer (2015), pp. 234-241

[16]: S. S. Bangaru, C. Wang, X. Zhou, M. Hassan, Scanning electron microscopy (SEM) image segmentation for microstructure analysis of concrete using U-net convolutional neural network, Automation in Construction, Volume 144, December 2022, 104602

[17]: K.-H. Ernst, J. Kirschner, Epitaxy: Physical Principles and Technical Implementation, 2004, Springer

[18]: J. W. Matthews and A. E. Blakeslee, Nucleation and growth of thin films, Journal of Crystal Growth, Volume: 27 [1], 118-125, (1974)

[19]: V. K. LaMer and R. H. Dinegar, Theory, Production and Mechanism of Formation of Monodispersed Hydrosols, J. Am. Chem. Soc., 1950, 72, 4847–4854.